

27 • The orientation of the central domain determines whether antithetic fault activity concentrates
28 along the entire width of the domain boundaries or not. In the first case, fault activity is
29 compartmentalized in distinct domains. In the second case (no or partial fault activity along
30 domain boundaries), the relative brittle strength contrast determines fault propagation, interaction
31 and/or linkage across the central domain.

32 These findings were compared with the intraplate fault systems of the NW Iberian Peninsula, which
33 shows synthetic and antithetic faults whose distribution is similar to those observed in our models.

34 **Keywords**

35 Strike-slip fault zone, Fault interaction, Fault linkage, Vertical brittle strength contrasts, Analogue
36 modelling

37

38 **1. Introduction**

39 The structural styles and the factors that control the geometry of strike-slip faults have been investigated in
40 detail in many studies (e.g., Riedel, 1929; Anderson, 1951; Deng et al., 1986; Sylvester, 1988; Dooley and
41 Schreurs, 2012; Hatem et al., 2017; Lefevre et al., 2020a; Visage et al., 2023). In nature, strike-slip fault
42 systems typically have complex architectures consisting of numerous segments separated by steps or of
43 anastomosing, linked fault zones (e.g., Aydin and Nur, 1982; Barka and Kadinsky-Cade, 1988; Wesnousky,
44 1988; Stirling et al., 1996; Kim et al., 2004). How faults interact or link is considered to be a function of
45 loading, stress disturbances, rheology and the geometry of pre-existing structures (e.g., Kim et al., 2004;
46 Myers and Aydin, 2004; Peacock and Sanderson, 1991, 1992; Burgmann and Pollard, 1994; Sibson, 1985;
47 Gamond, 1983; Rispoli, 1981; Wesnousky, 1988).

48 Understanding strike-slip fault interaction and linkage is important not only in view of the location of
49 geothermal and hydrocarbon resources (e.g. Sibson, 1985; Martel and Peterson, 1991; Aydin, 2000; Odling
50 et al., 2004; Cazarin et al., 2021) but also for its implications on regional stress orientations (Kirkland et
51 al., 2008), as well as seismic hazard (Petersen et al., 2011; Bullock et al., 2014), in terms of dynamics, fault
52 growth and size of earthquakes (e.g. Aki, 1989; Harris and Day, 1999; Scholz, 2002; Wesnousky, 2006;
53 Shaw and Dieterich, 2007; de Joussineau and Aydin, 2009; Preuss et al., 2019).

54 Various studies have investigated the influence of vertical changes in mechanical strength (e.g., a horizontal
55 sedimentary sequence comprising layers or bodies of different strengths) on strike-slip fault orientation,
56 segmentation, linkage, and displacement, using field observations, combined with analytical and numerical
57 methods (e.g. Du and Aydin, 1995; Aydin and Berryman, 2010; De Dontney et al., 2011), or analogue
58 models (Richard, 1991; Richard et al., 1995; Gomes et al., 2019; Gabrielsen et al., 2023; Venancio and
59 Alves Da Silva, 2023).

60 Strike-slip fault systems have large aspect ratios (i.e., ratio of length vs width) and can extend over hundreds
61 or even thousands of kilometres and often cut across pre-existing tectonic or lithological boundaries that
62 are steeply oriented and have rocks of contrasting mechanical strength on either side. Hence, it is also
63 important to understand the interaction between vertical domains of contrasting mechanical strength and
64 strike-slip faulting. To our knowledge no modelling studies have systematically investigated how strike-
65 slip fault systems are influenced by pre-existing steeply oriented domains with rocks of contrasting
66 mechanical strength on either side of the contacts. Such (sub)vertical contacts often occur at crustal terrane
67 boundaries, but also occur within crustal blocks comprising rock units of contrasting strength separated by
68 vertical boundaries, e.g. a magmatic body with steep margins that intruded into a sedimentary sequence.

69 Here we use scaled analogue model experiments analysed by PIV to assess the role of vertical domains of
70 contrasting brittle strength in the upper crust on fault kinematics in distributed strike-slip shear. Our results
71 show that the presence of such vertical domains with different strengths has a profound influence on the
72 kinematic evolution of strike-slip fault systems. We compare our experimental model results with a crustal-
73 scale example in the NW part of the Iberian Peninsula, where two large parallel and sinistral strike-slip
74 fault systems cut lithological domains of contrasting strength.

75

76 **2. Methods**

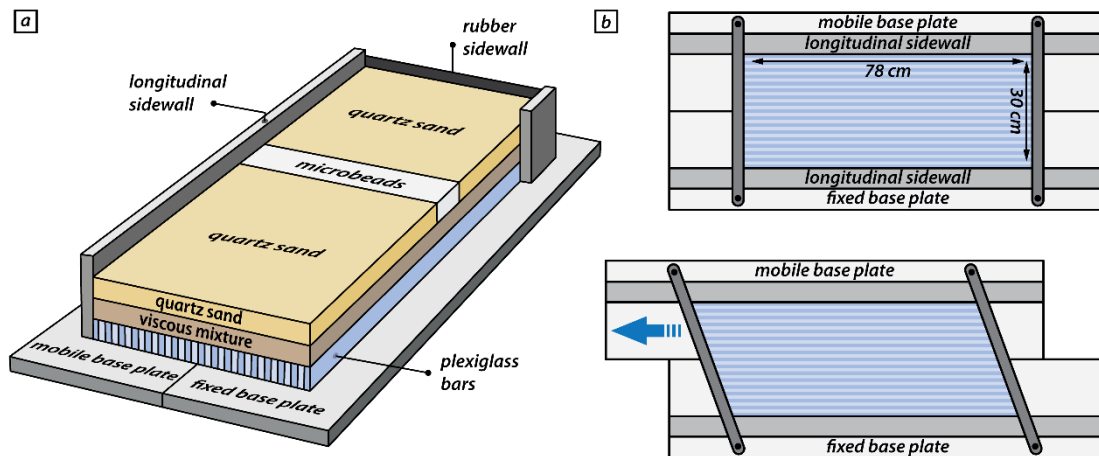
77 **2.1. Analogue model setup**

78 The experimental set-up for simulating distributed strike-slip shear included a mobile base plate that could
79 be translated horizontally past a fixed base plate (Fig. 1). An assemblage of 60 individual and moveable
80 plexiglass bars (each 78 cm long, 5 cm high and 5 mm wide) was positioned on top of two base plates. The
81 assemblage of plexiglass bars was confined by carbon-fiber sidewalls on the long sides (Fig. 1b) and
82 wooden bars (c. 5 mm high, 2 cm wide and 40 cm long) on the short sides (Fig. 1b, c), that could pivot

83 below the longitudinal sidewalls. The model was constructed on top of the plexiglass bars and consisted of
 84 a 2 cm-thick viscous layer, simulating the ductile lower crust, overlain by a 2 cm-thick layer of granular
 85 materials simulating the brittle upper crust. The short sides of the model were confined by vertical rubber
 86 sheets. Although our model set-up thus included both a horizontal viscous layer overlain by a horizontal
 87 brittle layer, our experiments focus on the influence of vertical domains with brittle strength contrasts on
 88 strike-slip faulting. The function of the viscous layer, directly overlying the plexiglass bars, is to distribute
 89 the applied shear deformation over the entire width of the model in the overlying brittle layer (e.g. Schreurs,
 90 1991, 2003; Dooley and Schreurs, 2012).

91 Each model had an initial rectangular shape in map view, with a length of 78 cm parallel to the shear
 92 direction and a width of 30 cm perpendicular to it. The movement of the mobile base plate occurred by
 93 computer-controlled stepper motors at a constant velocity of 40 mm/h, resulting in 80 mm of total
 94 displacement after two hours. Displacement of the mobile base plate changed the initial rectangular shape
 95 of the overlying assemblage of plexiglass bars into a parallelogram simulating simple shear.

96



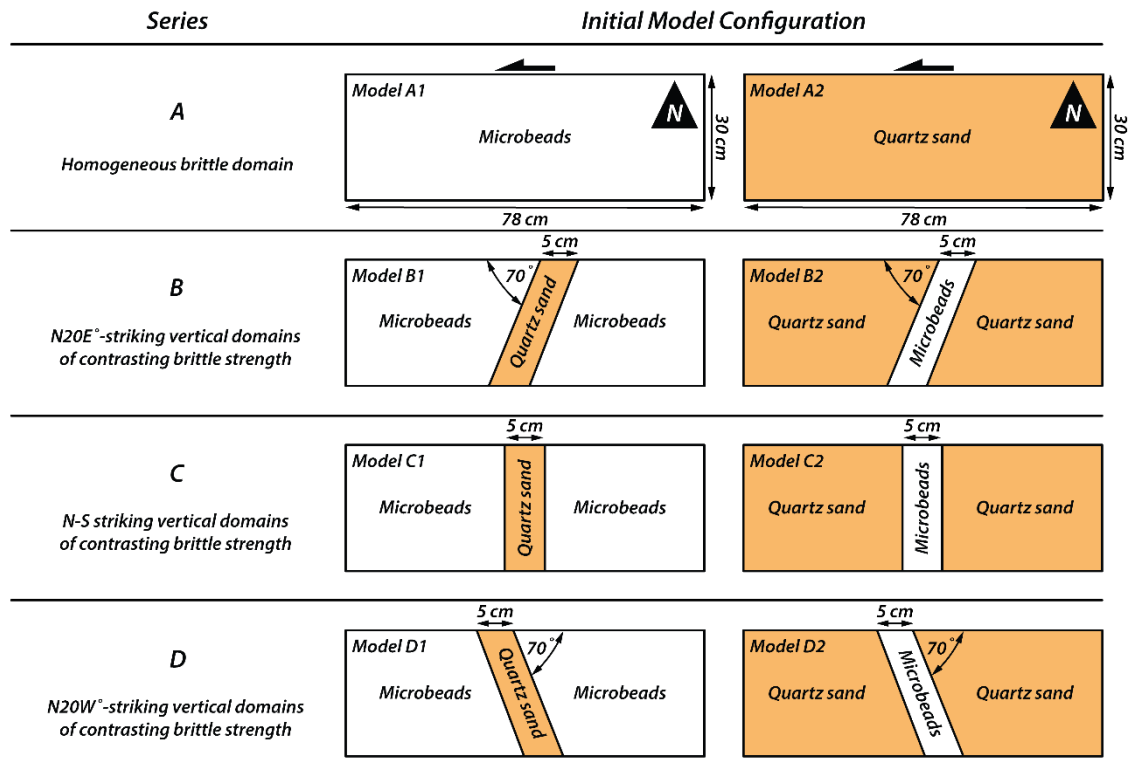
97

98 **Figure 1: Schematic experimental setup.** (a) The base of the model set-up consists of a fixed plate and a mobile
 99 plate overlain by an assemblage of individual and moveable plexiglass bars. The model is constructed on top of
 100 the plexiglass bars and is confined by two longitudinal sidewalls and two short sidewalls consisting of rubber
 101 sheets. (b) upper panel: Initial position of base plates overlain by plexiglass bars confined on the short sides by
 102 wooden bars that can pivot about a vertical axis; lower panel: Sinistral horizontal displacement of the mobile
 103 base plate induces a simple shear movement in the overlying assemblage of plexiglass bars as they slide past one
 104 another.

105

106 We performed four series of simple shear experiments, referred to as Series A, B, C and D (Fig. 2). Series
107 A involved two reference models with only one brittle material (Fig. 2a), either quartz sand or microbeads,
108 to investigate strike-slip fault kinematics in a homogeneous upper crust, without any lateral variations in
109 mechanical strength. In the subsequent three series (Fig. 2b-d), we introduced vertical domains that
110 consisted of quartz sand or microbeads. Each model had three domains with a c 5-cm-wide central domain
111 consisting of a different brittle material than the domains on either side. The difference between Series B,
112 C and D is the orientation of the central domain with respect to the shear direction, which changed from
113 one series to the next. To achieve such a model set-up, two vertical thin sheets of cardboard (< 1 mm) were
114 first placed as provisional walls, spaced 5 cm apart, on top of the viscous layer in the central domain of the
115 model, parallel to the required orientation of the vertical boundaries. Subsequently, the different granular
116 materials were sieved on top of the viscous layer and once the desired model thickness was reached, the
117 cardboard sheets were carefully removed. Although removal of the cardboard produced increased dilation
118 along a narrow zone, it hardly affects the de facto function of this vertical boundary as a primary surface
119 with materials of contrasting brittle strength on either side. For descriptive purposes, we defined a North
120 direction, which is perpendicular to the applied shear direction and parallel to the short sides of the
121 undeformed model (Fig. 2a). In models with a brittle strength contrast, we can distinguish two outer
122 domains, a western and an eastern one, and a central domain (Fig. 2b-d).

123



124

125

Figure 2: Schematic top views of the four series of models, with dimensions and brittle analogue materials used

126

127 2.2. Analogue materials

128

We used two different types of granular materials in our analogue models to assess the role of vertical zones of contrasting mechanical strength in the upper crust: quartz sand and microbeads grains. The quartz sand (distributor Carlo Bernasconi AG; www.carloag.ch) has a grain size between 60 and 250 μm with a bulk density of 1560 kg m^{-3} , whereas the grain size of the microbeads (distributor: Worf Glasskugeln, Germany) lies between 150 and 210 μm with a bulk density of 1400 kg m^{-3} . These density values were achieved by sieving the granular material into the model box from a height of 30 cm. Both, quartz sand and microbeads deform according to the Coulomb failure criterion and have internal peak friction angles of 36° and 22° and cohesion values of 50 ± 26 Pa and 25 ± 4 Pa, respectively (Panien et al., 2016; Schmid et al., 2020). The considerable difference in the internal peak friction angle between the two materials makes them suitable for simulating contrasting upper crustal rocks. According to their difference in the internal friction angle, we consider the microbeads and quartz sand as weak and strong materials, respectively.

139

The viscous layer in our models had a density of 1600 kgm^{-3} and consisted of a mixture of SGM-36 polydimethylsiloxane (PDMS) and corundum sand (weight ratio of 0.965: 1.000). The mixture has a quasi-

140

141 linear viscosity of 1.5×10^5 Pa s and a stress exponent of 1.05 (Zwaan et al., 2018). The properties of all
 142 analogue materials are summarized in Table 1.

143

144

Granular materials	Quartz sand	Microbeads	Viscous material	PDMS/corundum mixture
Density (kg/m ³)	1560	1400	Density (kg/m ³)	1600
Grain size (μm)	60-250	150-210	Viscosity (Pa s)	1.5×10^5
Peak friction coefficient μ and angle, ϕ	0.72 - 36°	0.41 - 22°	Stress exponent n	1.05
Cohesion (Pa)	50 ± 26	25 ± 4		

145 **Table 1:** Materials properties of used granular and viscous materials (after Panien et al., 2006; Schmid et al., 2020).

146

147

148 2.3. Scaling

149 For brittle Mohr-Coulomb type materials, dynamic similarity is given by the equation for stress ratios

$$\sigma^* = \rho^* g^* h^* \quad (1),$$

150 where ρ^* , g^* and h^* are the ratios of model to nature for density, gravity and length, respectively. Note,
 151 that our two used granular materials have different densities, cohesions and internal friction coefficients.
 152 However, the resulting scaling factors are nearly identical and therefore we provide only the scaling factors
 153 for quartz sand. Where scaling factors substantially differ, we denote them with subscripts “qtz” and “mb”
 154 for quartz sand and microbeads, respectively. Our model setup yields a length scaling factor of $h^* =$
 155 2×10^{-6} and a gravity scaling factor of 1. For quartz sand, the density scaling factor is $\rho_{qtz}^* \sim 0.6$ and the
 156 cohesion factor is $C_{qtz}^* = 1 \times 10^{-6}$ (using a cohesion of ~50 Pa and 50 MPa for our quartz sand and upper
 157 crustal rocks, respectively; Byerlee, 1978). Additionally, for microbeads the density scaling factor and
 158 cohesion scaling factor are $\rho_{mb}^* \sim 0.5$ and $C_{mb}^* = 1 \times 10^{-6}$ (assuming a weakened natural rock type with a

159 cohesion of c. 25 MPA), respectively. Using these scaling factors yields a stress scaling factor of $\sigma^* =$
160 1×10^{-6} for both quartz sand and microbeads.

161 Assuming a lower crustal viscosity of $\eta = 10^{22}$ Pa s (Moore and Parsons, 2015; Zhang and Sagiya, 2017)
162 yields a viscosity ratio $\eta^* = 1 * 10^{-17}$ (using the viscosity of $1.5 * 10^5$ Pa s for the viscous analogue
163 material).

164 The strain rate ratio is obtained from the stress ratio and the viscosity ratio by (Weijermars and Schmeling,
165 1986):

$$\dot{\epsilon}^* = \frac{\sigma^*}{\eta^*} \quad (2).$$

166 Note that due to the simple shear setup, we substitute the strain rate scaling factor $\dot{\epsilon}^*$ with the shear strain
167 rate scaling factor $\dot{\gamma}^* = 1 \times 10^{11}$. Next, the velocity scaling factor v^* and a time scaling factor t^* are
168 calculated with

$$\dot{\gamma}^* = \frac{v^*}{h^*} = \frac{1}{t^*} \quad (3)$$

169 yielding a velocity scaling factor $v^* = 2 \times 10^5$ and a time scaling factor $t^* = 1 \times 10^{-11}$.

170 Based on our scaling, 1 cm in our experiments corresponds to 5 km in nature and the applied velocity of 40
171 mm h⁻¹ converts to a velocity of ~2 mm a⁻¹ in nature. Using the shear strain rate scaling factor $\dot{\gamma}^*$, the bulk
172 shear strain rate $\dot{\gamma} = 3.7 \times 10^{-5} \text{ s}^{-1}$ in our models translates to a shear strain rate of $\dot{\gamma} = 3.7 \times 10^{-16} \text{ s}^{-1}$
173 in nature and 1 h in our analogue experiments translates to ~12.5 Myr in nature.

174 In order to verify dynamic similarity of brittle natural and experimental material we calculate the
175 Smoluchowski number S_m , which is the ratio between gravitational stress and cohesive strength (Ramberg,
176 1981):

$$S_m = \frac{\rho g h}{C + \mu \rho g h} \quad (4),$$

177 where ρ , h , C and μ are the density, thickness, cohesion, and friction coefficient, respectively of the brittle
 178 material. With a cohesion of 50 MPa and a friction coefficient of ~0.6 (Byerlee, 1978) for upper crustal
 179 rocks, this yields values of $S_m \sim 1$ for our models as well as for nature. We further calculate the Ramberg
 180 number R_m to ensure dynamic and kinematic similarities between the viscous layers.

$$R_m = \frac{\rho g h^2}{\eta v} \quad (5)$$

181 For our velocity of 40 mm h⁻¹, this yields a Ramberg number of 6 for both, our models and nature. The
 182 Reynolds number R_e is defined as the ratio between inertial forces and viscous forces and is for all our
 183 models as well as for the natural prototype $\ll 1$:

$$R_e = \frac{\rho v h}{\eta} \quad (6)$$

184 Based on the applied scaling laws, the material properties and the similar non-dimensional numbers for
 185 model and nature, we consider our models to be properly dynamically scaled. Model parameters and
 186 dynamic numbers of the used materials are specified in Table 2.

187

	General parameters			Brittle upper crust		Ductile lower crust		Dimensionless numbers		
	Gravity [m/s ²]	Crustal thickness [m]	Shear velocity [m/s]	Density [kg/m ³]	Cohesion [Pa]	Density [kg/m ³]	Viscosity [Pa s]	Smoluchowski Sm	Ramberg Rm ¹	Reynolds Re
Model	9.81	4 x 10 ⁻²	1.1 x 10 ⁻⁶	1560	50	1600	1.5 x 10 ⁵	1	6	$\ll 1$
Nature	9.81	2 x 10 ⁴	6.3 x 10 ⁻¹¹	2700	5 x 10 ⁷	2900	1 x 10 ²²	1	6	$\ll 1$
Scaling ratios $x^* = x^m/x^n$ [dimensionless]										
	σ^*	ρ^*	g^*	h^*	C^*	$\dot{\gamma}^*$	η^*	v^*	t^*	
	1 x 10 ⁻⁶	0.5 ¹ -0.6	1	2 x 10 ⁻⁶	5 ¹ -10 x 10 ⁻⁷	1 x 10 ¹¹	1 x 10 ⁻¹⁷	2 x 10 ⁵	1 x 10 ⁻¹¹	

188 ¹ Lower values for scaling factors ρ^* and C^* refer to microbeads.

189 **Table 2:** Scaling parameters and scaling factors.

190

191

192

193

194 2.4. Deformation monitoring and quantification

195 Since the experiments were conducted using a simple shear setup, vertical motions during deformation
196 were negligible, with nearly all movement located within the horizontal plane. The different experiments
197 were monitored by an automated Nikon D810 (36 MPx) DSLR camera positioned above the experimental
198 model. Images were taken at fixed intervals of 60 s during two hours, resulting in 121 subsequent top view
199 images of the model surface. For a quantitative 2D analysis of the surface deformation, we used the
200 StrainMaster module of the LaVision© DaVis image correlation software. Using a calibration plate, the
201 software corrects the top view images for lens distortion effects (i.e., unwarping), applies image
202 rectification and provides a scaling function that maps coordinates from the camera sensor to physical world
203 coordinates with a resolution of ~ 9 px/mm. The digital image correlation calculates local displacement
204 vectors on subsequent images using a square matching algorithm with adaptive multi-pass cross-
205 correlation. To properly track freckle patterns, we sprinkled coffee grains on the model surface prior to the
206 model run. For each image, the analyzed area is subdivided into small interrogation window for which a
207 local displacement vector is determined by cross-correlation. We used subsets (i.e., interrogation windows)
208 of 31 by 31 pixels with a 75% overlap for the local displacement calculations that, assembled result in
209 incremental (60 s interval) displacement fields for the horizontal x- and y-components u_x and u_y ,
210 respectively with a vector resolution of ~ 1.3 vectors/mm.

211 Postprocessing included an outlier filter to fill gaps of pixels within a 3 by 3 neighborhood (Westerweel
212 and Scarano, 2005). Discarded vectors in the displacement fields were replaced by an iterative interpolation
213 requiring at least two neighboring vectors. For quantifying deformation at the model surface, we calculate
214 the z-vorticity ω_z (i.e., a local measure of rotation within the xy-plane) as a proxy for shear movement
215 along strike-slip faults. In contrast to the shear strain ε_{xy} , vorticity is not dependent on the orientation of
216 the coordinate system, which is crucial when quantifying deformation along faults that strike obliquely with
217 respect to the coordinate system (e.g., Cooke et al., 2020). ω_z can be derived from local displacement
218 gradients according to equation 1:

$$\omega_z = \frac{\partial u_y}{\partial x} - \frac{\partial u_x}{\partial y} \quad (7)$$

219 With u_x and u_y being the horizontal displacement components in the x, and y direction, respectively. Due
220 to convention, positive and negative ω_z values refer to sinistral and dextral relative displacement,
221 respectively. Within the predefined increment of 60 s, ω_z values are consistently within the range [-2%,
222 2%] and we set a threshold of -0.5% and 0.5% to distinguish between active deformation and background
223 noise for dextral and sinistral shear sense, respectively. In the results section we present ω_z at deformation
224 stages every 30 min (i.e., after 30, 60, 90, and 120 min). Finite deformation after 120 min for each model
225 is illustrated with a surface photograph and enhanced with superposed line drawings of the fault pattern.
226 For the statistical analysis of fault orientations, we traced active fault segments (i.e., $\omega_z \leq -0.5\%$ or $\omega_z \geq$
227 0.5%) in MATLAB using polylines, where each fault segment is defined by two consecutive vertices. At
228 each time step, segment length and azimuth were calculated and visualized in length-weighted rose
229 diagrams.

230

231 **3. Results**

232 We present the results of eight distributed strike-slip shear experiments, grouped in four series of two
233 models each. Series A models included two reference models having a homogeneous upper brittle layer,
234 whereas Series B, C and D models had vertical domains with contrasting brittle strengths (Fig. 2).

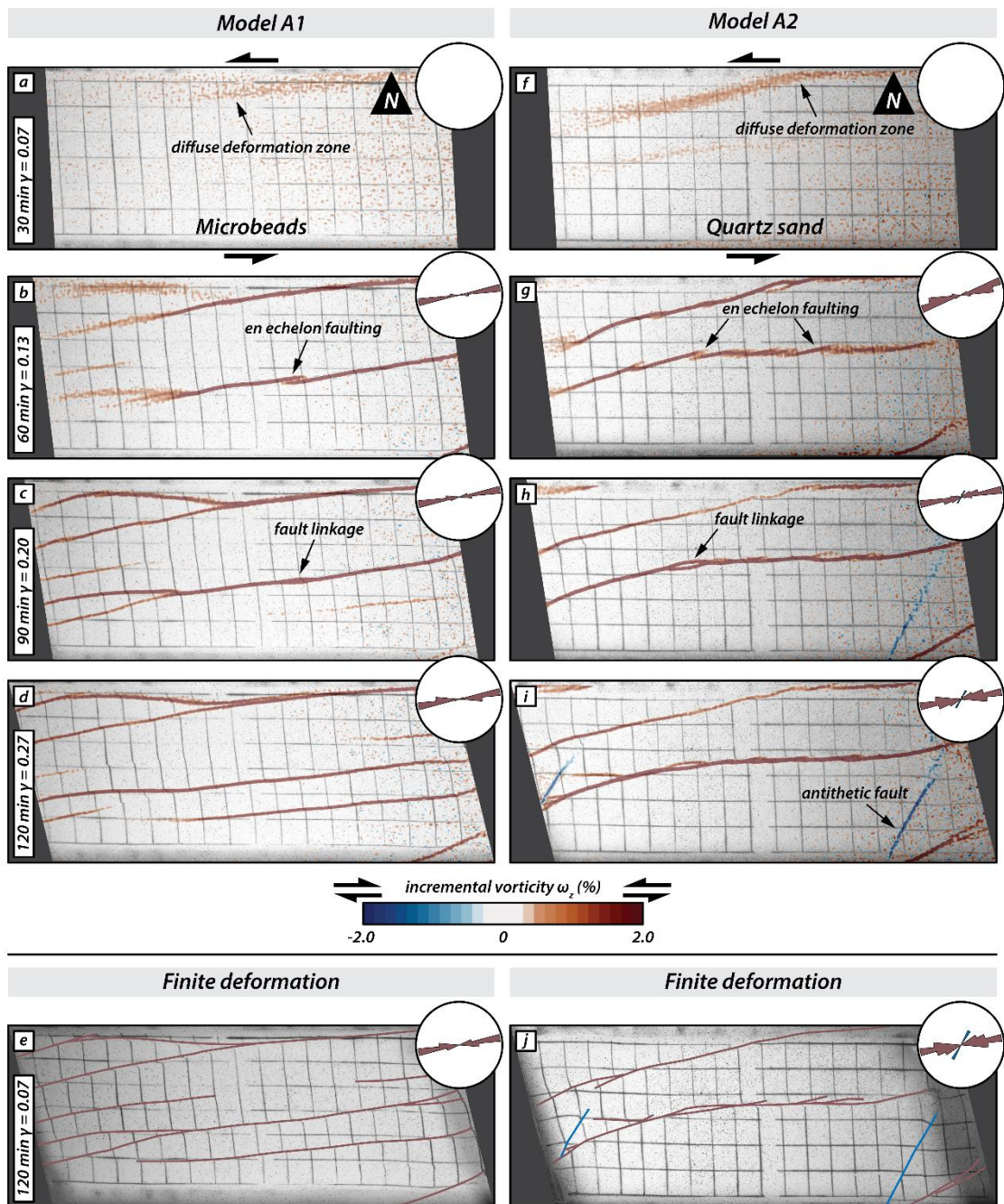
235

236 **3.1. Series A: Fault evolution in a homogeneous upper crust**

237 The Series A models consisted of a homogeneous upper crustal layer composed of either microbeads (Fig.
238 3; Model A1) or quartz sand (Fig. 3; Model A2). The incremental strain panels document that strain
239 localized first in the model with quartz sand, while deformation was still diffuse in the model with
240 microbeads (Fig. 3a and f), i.e. strain localization occurs at lower amounts of applied simple shear in quartz
241 sand than in microbeads. With progressive sinistral simple shear deformation, slightly overlapping right-
242 stepping *en echelon* strike-slip faults with a sinistral displacement formed (Fig. 3b and g). These faults were
243 synthetic with respect to the bulk simple shear. In the model with microbeads (Model A1) the first synthetic
244 faults had an orientation of c. N79°E (Fig. 3b), whereas in the model with quartz sand (Model A2) their
245 orientation was c. N72°E (Fig. 3g). Initial deformation in both models is accommodated by synthetic
246 (sinistral) strike-slip faults only (Fig. 3a, b and f, g). As deformation progressed, individual fault segments

247 linked up forming major sinistral strike-slip faults (Fig 3c and h). Antithetic faults only developed in Model
 248 A2 (quartz sand only; Fig. 3h and i) at later stages of deformation. These faults were confined in between
 249 previously formed synthetic faults. The final deformation stage (Fig. 3e and j) shows that most deformation
 250 was taken up by major synthetic faults that crossed the entire length of the model. At the final stage, the
 251 initial *en echelon* pattern of faulting was better preserved in the quartz sand model than in the microbeads
 252 model, resulting in a wider damage zone in the former.

253



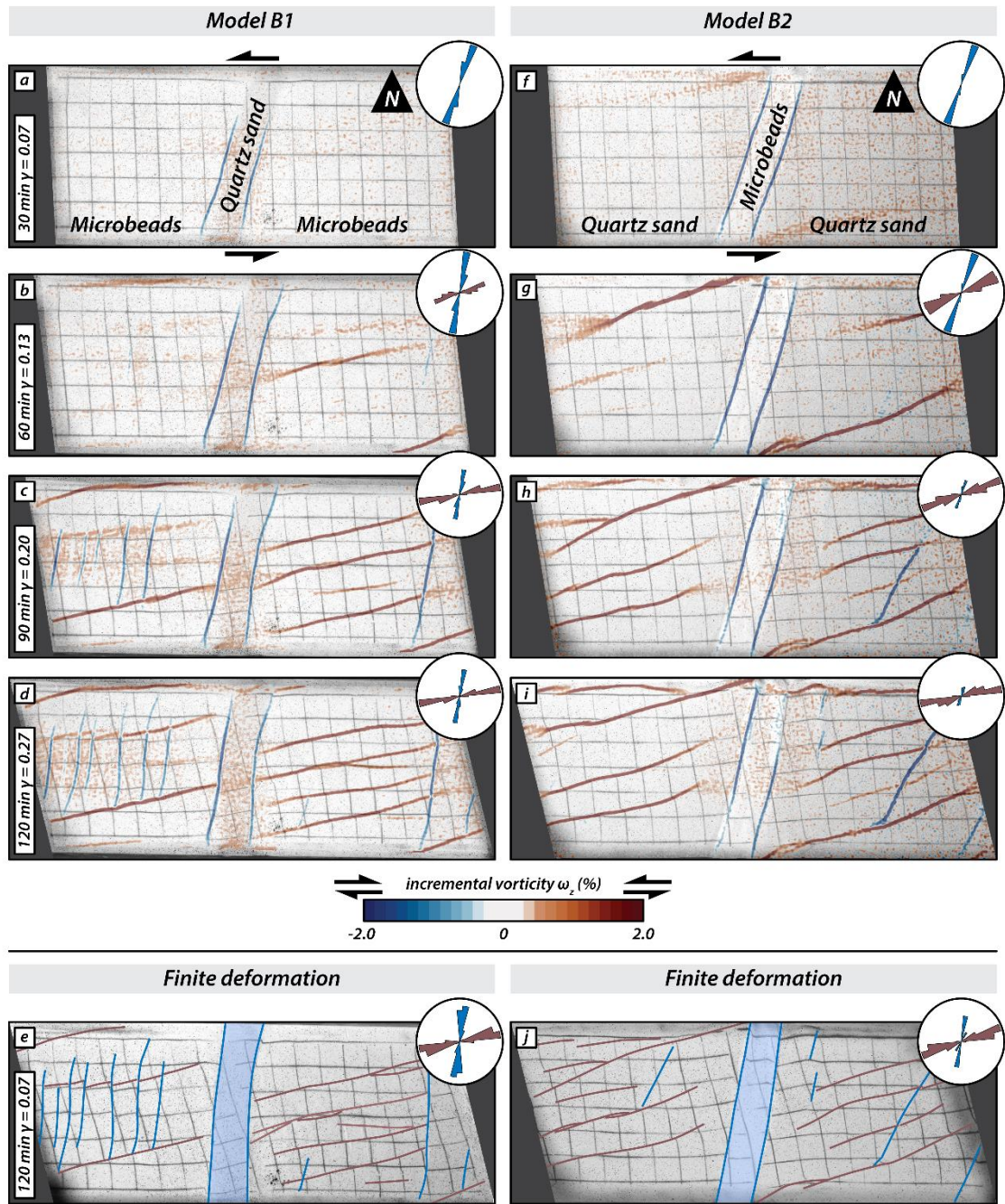
254

255 **Figure 3: Overview of Series A models: Simple shear deformation of two models with a homogenous upper**
256 **brittle layer. The first four panels of each series show surface photographs with the incremental vorticity after**
257 **30 minutes (20 mm displacement of mobile base plate), 60 minutes (or 40 mm displacement), 90 minutes (or 60**
258 **mm displacement) and 120 minutes (or 80 mm displacement). Incremental positive and negative values indicate**
259 **sinistral (synthetic, red) and dextral (antithetic, blue) relative movement, respectively. The last panel for each**
260 **series shows a surface photograph of the final stage overlain with the interpreted fault pattern; red lines are**
261 **sinistral faults, blue lines are dextral faults.**

262

263 **3.2. Series B: Fault evolution in models with N20°E vertical domain boundaries**

264 The vertical domain boundaries in the Series B models were oriented N20°E. Model B1 had a central
265 domain consisting of strong quartz sand with weak microbeads in the adjacent, western and eastern domains
266 (Fig. 4; Model B1), whereas in Model B2 it was the other way around. (Fig. 4; Model B2). Both models
267 showed the development of dextral strike-slip (antithetic, with respect to sinistral simple shearing) faults
268 along the vertical boundaries of the central domain (Fig. 4a, f). Slightly later, sinistral strike-slip faults
269 (synthetic) formed in the western and eastern domains (4b, g). Although these faults propagated laterally
270 with time, none of the synthetic faults crossed the central domain. Instead, they halted at or close to the
271 boundary faults along the central domain (Fig. 4c, h). In Model B1 a few antithetic faults formed in between
272 pre-existing synthetic faults in the outer domains, striking at c. N60°E (Fig. 4d, e). Antithetic faults
273 developed also in the western and eastern domains of Model B2, almost coevally with the synthetic faults.
274 They strike at higher angles to the shear direction than those antithetic faults confined between overlapping
275 synthetic faults in Model B2. With increasing deformation, the central domain and its bordering antithetic
276 faults rotated counterclockwise in both models (Fig. 4a-e, f-j), as did the antithetic faults in the western and
277 eastern domains, which acquired a slight sigmoidal “S-shaped” form (e.g. Fig. 4j)



278

279 **Figure 4: Overview of Series B models: Simple shear deformation of two models with vertical domains of contrasting brittle strength oriented N20°E. The first four panels of each series show surface photographs with the incremental vorticity after 30 minutes (20 mm displacement of mobile base plate), 60 minutes (or 40 mm displacement), 90 minutes (or 60 mm displacement) and 120 minutes (or 80 mm displacement). Incremental positive and negative values indicate sinistral (synthetic, red) and dextral (antithetic, blue) relative movement, respectively. The last panel for each series shows a surface photograph of the final stage overlain with the interpreted fault pattern; red lines are sinistral faults, blue lines are dextral faults.**

286

287

288

289

290

3.3. Series C: Fault evolution in models with N-S vertical domain boundaries

291

The Series C models had vertical N-S striking domain boundaries. Model C1 had a 5-cm wide central

292

domain of quartz sand with microbeads on either side (Fig. 5; Model C1), whereas in Model C2 it was the

293

other way around (Fig. 5; Model C2). During the early stages of simple shear, dextral (antithetic) faults

294

formed along the N-S striking borders of the central domain (Fig. 5b, g) in both models, but earlier and

295

more pronounced in Model C1. With progressive shearing, both synthetic and antithetic faults formed in

296

the outer domains of both models (Fig. 5c and h). In Model C2, activity along the antithetic faults bordering

297

the central domain ceased, and synthetic faults propagated from the outer domains into the central weak

298

domain (Fig. 5h-j). In contrast, in Model C1, the antithetic faults along the borders of the central domain

299

remained active, and no synthetic faults crossed the central strong domain (Fig. 5d). In the eastern domain

300

of Model C2, a few antithetic faults formed in between major synthetic faults, striking at a lower angle to

301

the shear direction than earlier formed antithetic faults in the western domain. With progressive simple

302

shear the central domain showed counterclockwise rotation about a vertical axis in both models and

303

antithetic faults obtained a sigmoidal shape as seen in top view (Fig. 5i). As the initial N-S antithetic faults

304

bordering the central domain rotated counterclockwise, activity along these faults diminished and new fault

305

segments appeared striking nearly parallel to earlier formed antithetic faults in the western and eastern

306

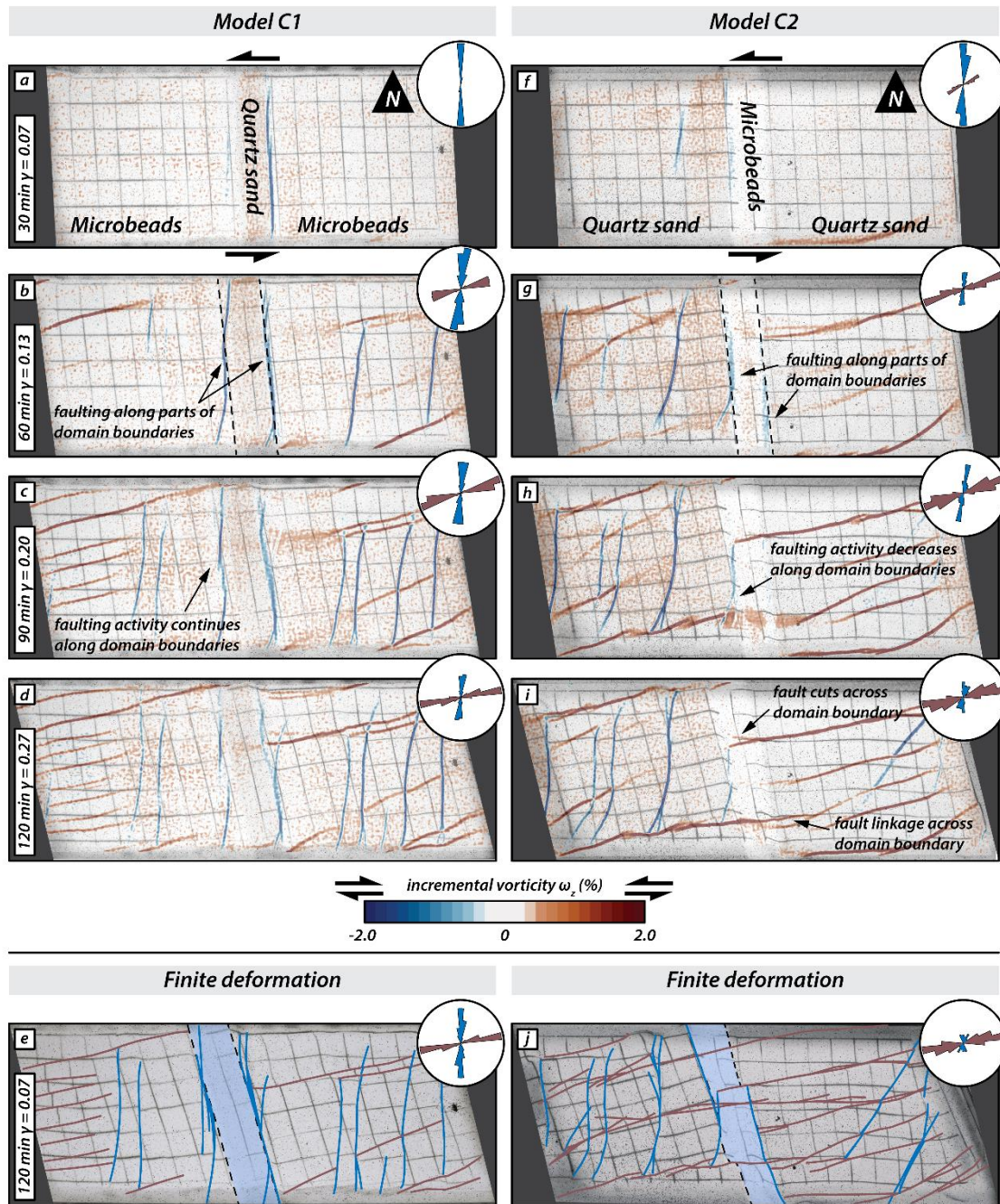
domain (Fig. 5d, e). At the final stage of Model C2, antithetic faults dominated in the western domain and

307

synthetic faults in the eastern domain. In contrast, in Model C1, both antithetic and synthetic faults were

308

present in both the western and eastern domain.



309

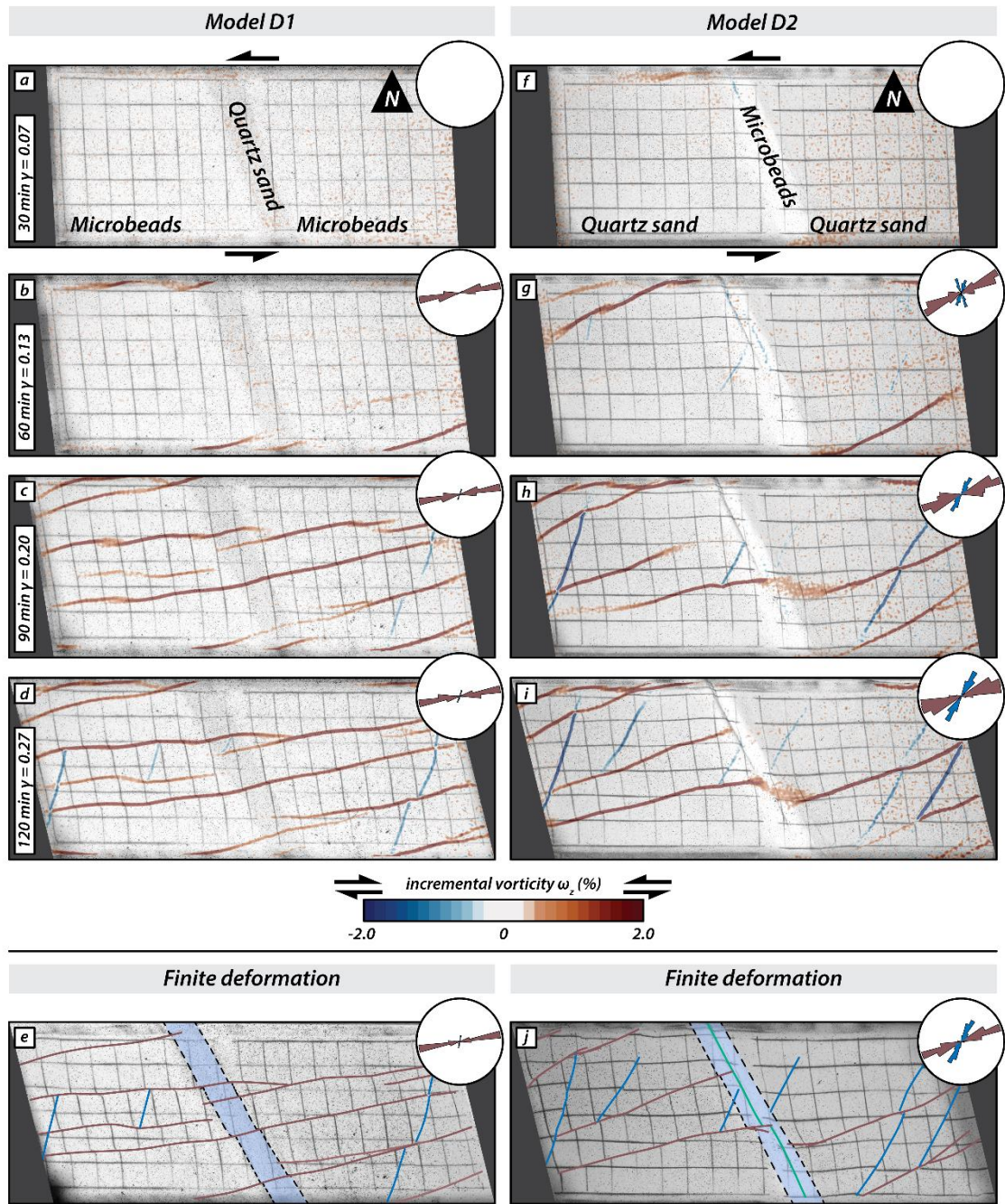
310 **Figure 5: Overview of Series C models: Simple shear deformation of two models with vertical domains of**
 311 **contrasting brittle strength striking N-S. The first four panels of each series show surface photographs with the**
 312 **incremental vorticity after 30 minutes (equivalent to 20 mm displacement of the mobile base plate), 60 minutes**
 313 **(or 40 mm displacement), 90 minutes (or 60 mm displacement) and 120 minutes (or 80 mm displacement).**
 314 **Incremental positive and negative values indicate sinistral (synthetic, red) and dextral (antithetic, blue) relative**
 315 **movement, respectively. The last panel for each series shows a surface photograph of the final stage overlain by**
 316 **the interpreted fault pattern; red lines are sinistral faults, blue lines are dextral faults.**

317

318

319 **3.4. Series D: Fault evolution in models with N20°W striking vertical domain boundaries**

320 In the series D models the orientation of the vertical central domain was N20°W. In Model D1 the central
321 domain consisted of a 5 cm-wide central band of quartz sand with microbeads on either side (Fig. 6; Model
322 D1), whereas in Model D2 it was the other way around (Fig. 6; Model D2). In contrast to the Model C
323 series, no faults formed along the boundaries of the central domain in both Models D1 and D2 (Fig. 6a and
324 f). Model D1 is dominated by synthetic faults crosscutting the central strong domain (6c-e). As these faults
325 traversed the central domain, they slightly changed their strike orientation. In contrast, in Model D2 the
326 weak microbeads of the central domain were internally deformed and oblique-slip reverse faults formed,
327 which propagated laterally and parallel to the domain boundaries (Fig. 6g-j). Synthetic faults formed both
328 in the western and eastern domain of Model D2, while antithetic faults formed later and in between
329 overlapping synthetic faults (Fig. 6g-j). With progressive deformation synthetic faults from the western and
330 eastern domain in Model D2 propagated partially into the central, weak domain, but halted at the previously
331 formed oblique-slip reverse faults (Fig. 6h and i). During late stages of deformation a few antithetic faults
332 formed in Model D1 in between earlier formed synthetic faults, striking at somewhat larger angles to the
333 shear direction than in Model D2.



334

335 **Figure 6: Overview of Series D models: Simple shear deformation of two models with N20°W striking vertical**
 336 **domains of contrasting brittle strength. The first four panels of each series show surface photographs with the**
 337 **incremental vorticity after 30 minutes (20 mm displacement of mobile base plate), 60 minutes (or 40 mm**
 338 **displacement), 90 minutes (or 60 mm displacement) and 120 minutes (or 80 mm displacement). Incremental**
 339 **positive and negative values indicate sinistral (synthetic, red) and dextral (antithetic, blue) relative movement,**
 340 **respectively. The last panel for each series shows a surface photograph of the final stage overlain with the**
 341 **interpreted fault pattern; red lines are sinistral faults, blue lines are dextral faults.**

342

343

344

345

346 **4. Discussion**

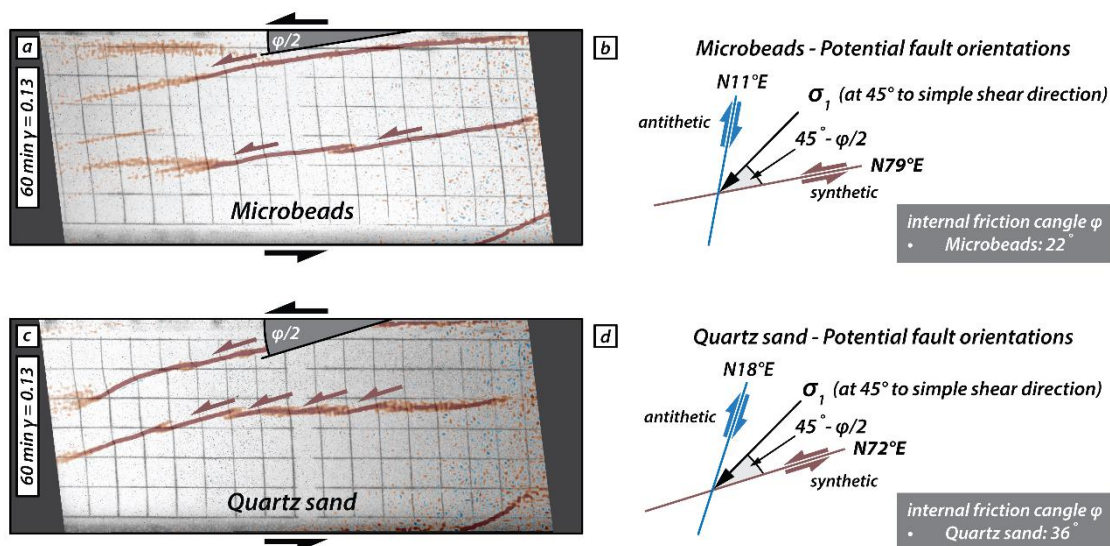
347 We performed analogue modelling experiments to test the influence of vertical, upper crustal domains of
348 contrasting strength on the development and evolution of strike-slip fault zones. We first discuss the fault
349 kinematics of two reference models which simulated a uniform upper, brittle crust (section 4.1).
350 Subsequently, we discuss and compare the results of three series of models (Series B, C and D, in which
351 two different brittle materials, strong quartz sand and weak microbeads, alternated to form three vertical
352 domains of contrasting strength (section 4.2), i.e. either weak-strong-weak (i.e. quartz sand-microbeads-
353 quartz sand) or strong-weak-strong (i.e. microbeads-quartz sand-microbead section). Each of these three
354 series had a different orientation of the vertical domains with respect to the shear direction. In section 4.3
355 we discuss how the central vertical domain affects fault interaction and/or fault linkage. In the final section
356 4.4 we compare modelling results with a strike-slip fault system in the Iberian Peninsula.

357 **4.1. Series A: Strike-slip faulting in models with a homogeneous upper brittle layer**

358 Initial bulk simple shear is accommodated in both models by zones of diffuse deformation and is followed
359 by localized deformation along narrow fault zones. It is interesting to note that localization requires a higher
360 shear deformation in the model with the weak microbeads than in the model with quartz sand. This
361 difference in localization behaviour is attributed to the difference in dilatancy between the two analogue
362 materials, which is closely related to grain shape and grain size distribution. The microbeads are well-
363 rounded and have a narrow grain size distribution (150-210 μm), whereas the quartz sand grains are angular
364 and have a wider grain size distribution (60-250 μm). The more equal the grain shape and grain size, the
365 more applied shear deformation is needed before strain localizes along a narrow fault zone (Antonellini et
366 al., 1995; Mair et al., 2002).

367 Sinistral (synthetic) strike-slip faults form in both models. The initial strike of these faults differs between
368 the model with microbeads and the one with quartz sand, striking at c. N79°E and N72°E, respectively. The
369 synthetic fault orientations reflect the Mohr-Coulomb fracture criterion for faulting in a homogeneous
370 material (Fig. 7). At the onset of simple shear, the main principal stress, σ_1 is oriented at 45° to the shear
371 direction, and the two potential fault orientations strike at $45^\circ - \phi/2$ and at $45^\circ + \phi/2$ to σ_1 , respectively
372 with ϕ the angle of internal peak friction i.e. the synthetic and antithetic faults would strike at N79°E and
373 N11°E, respectively in the model with microbeads and at N72°E and N18°E, respectively in the model with

374 quartz sand. In our models only the synthetic faults form during the early stages of simple shear
 375 deformation. The early synthetic faults form a right-stepping *en echelon* fault pattern that link up with
 376 increasing deformation to form major strike-slip faults. The fact that nearly all deformation is taken up by
 377 synthetic faults is typical of simple shear models with an initial rectangular shape, i.e. a large aspect ratio
 378 of length (parallel to shear direction) divided by width (Schreurs, 2003; Dooley & Schreurs, 2012). A
 379 comparison of previous simple shear experiments shows that the shape of the initial model has a clear
 380 influence on the relative proportion of synthetic and antithetic faults (Gapais et al., 1991; Schreurs, 2003).
 381 With decreasing aspect ratio, the number of antithetic faults will increase, and in case of an initially square-
 382 shaped model, (i.e., aspect ratio is 1) antithetic faults will dominate (Gapais et al., 1991; Dooley &
 383 Schreurs, 2012). In the model with quartz sand, a few antithetic faults form in between previously formed
 384 major synthetic faults (Fig. 3i). These late antithetic faults, however, form in response to local stress field
 385 modifications between overlapping synthetic faults, causing σ_1 to rotate clockwise from 45° to the bulk
 386 shear direction towards an orientation that is subparallel to the previously formed synthetic faults. As a
 387 consequence, these late antithetic faults are not in the “conjugate” position with respect to the synthetic
 388 major faults, but strike at lower angles with respect to the long borders of the model (these are the lower-
 389 angle antithetic faults of Schreurs, 2003).

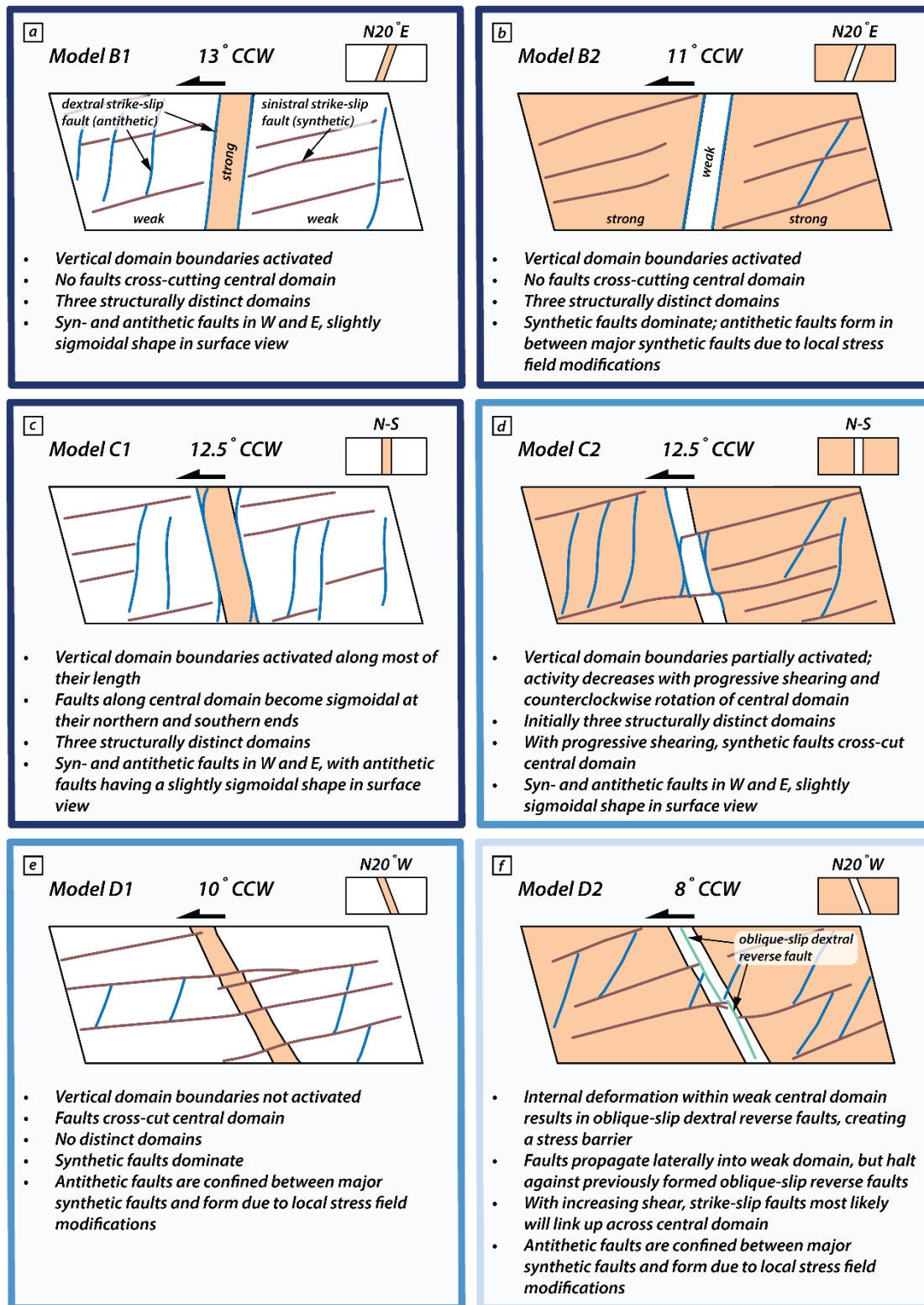


390

391 **Figure 7: Illustrative scheme of the expected fault orientation according to the Mohr-Coulomb failure criteria,**
 392 **for the experiments with only one type of material (homogeneous upper crust). a) and c) Surface photographs**
 393 **of the model with microbeads only (a) and quartz sand only (c), with the incremental vorticity after 60 minutes**
 394 **(40 mm displacement). b) and d) Schematic explanation for the expected orientation of the synthetic and**
 395 **antithetic faults considering the simple shear orientation along with the Mohr-Coulomb failure criteria, for the**
 396 **models with microbeads and quartz sand only respectively.**

397 **4.2. Series B, C and D: The influence of the orientation of vertical domains of contrasting**
398 **brittle strength on strike-slip faulting**

399 Introducing vertical domains of contrasting brittle strength in our models results in fault patterns that differ
400 when compared to the Series A models that consisted only of one homogeneous brittle material. The degree
401 of difference in the fault pattern is a function of the orientation of the vertical domains and whether the
402 domains have a strong (quartz sand) or weak (microbeads) material in the central domain. Fig. 8 shows a
403 schematic overview of the final structures of all six models which had vertical domains of contrasting brittle
404 strength. Each of these six models had an initial rectangular shape and consisted of a western, central and
405 eastern domain with the central one having a contrasting brittle strength with respect to the adjacent, outer
406 domains. The initial strike of the vertical domain boundaries, either N20°E, N-S or N20°W has a profound
407 influence on the resulting fault pattern.



408

409 Figure 8: Schematic surface views summarizing the main results from the models with vertical domains of
 410 contrasting brittle strength.

411

412 The domain boundaries in Series B models initially strike N20°E, which is close to the antithetic fault
413 orientation predicted by the Mohr-Coulomb failure criterion (i.e. N11°E for microbeads and N18°E for
414 quartz sand, see section 4.1). As a result the domain boundaries in both models are activated along their
415 entire length, forming antithetic, dextral strike-slip faults along them (Fig. 8a,d). With progressive sinistral
416 simple shear, the central fault-bounded domain rotates counterclockwise about a vertical axis, and at the
417 end of the experiment has rotated by about 12° striking c. N08°E. The domain boundaries remain active
418 throughout the model run, because their strike orientation remains close to the antithetic fault orientation
419 predicted by the Mohr-Coulomb failure criterion (Fig 8a, b). As a result of continuous fault activity along
420 the central domain boundaries, each of the two Series D models develops three spatially separated structural
421 domains: a western and eastern domain, containing both synthetic and antithetic faults, separated from a
422 central domain bordered by antithetic faults. Faulting is thus compartmentalized within the model and no
423 faults propagate from the outer domains into the central domain (Fig. 8a, b).

424 In comparison to the Series B models, the initial N-S strike of the central domain boundaries in the Series
425 C models (Fig 8c, d) is less favorably oriented with respect to the antithetic fault orientations predicted by
426 the Mohr-Coulomb failure criterion. As a result, the domain boundaries in both models are only partially
427 activated dextrally during initial simple shear deformation (Fig. 4). During progressive shearing the domain
428 boundaries rotate counterclockwise and become even less favorably oriented for further activation and fault
429 branches partially no longer follow the domain boundaries, with the overall fault geometry at and in the
430 vicinity of the central domain boundaries acquiring an overall “S-shaped” geometry in surface view (Fig.
431 8c, d). The difference between Model C1 (weak-strong-weak) and Model C2 (strong-weak-strong) is that
432 in the former the total length of the domain boundaries activated is larger and faults at or in the immediate
433 vicinity of the domain boundaries remain longer active than in the latter (compare Fig. 8c and d). This
434 difference can be explained by the fact that in Model C1 the weak microbeads represent the dominant brittle
435 material, and the antithetic fault orientation predicted by Mohr-Coulomb, N10°E for a homogeneous
436 microbeads layer, is close to the initial N-S orientation of the domain boundary. In contrast, Model C2 is
437 dominated by quartz sand and the antithetic fault orientation predicted by Mohr-Coulomb, N18°E for a
438 homogeneous quartz sand layer, is farther away from the initial N-S striking central domain and
439 consequently domain boundaries are less activated and fault activity decreases more rapidly with
440 progressive deformation. As a consequence in Model C2, synthetic faults forming in the outer domains can
441 propagate across the poorly activated domain boundaries, cross-cutting the central domain, and can partly

442 link up to form major through-going faults. In Model C1, however, fault activity along domain boundaries
443 was stronger and occurred longer, and the domain boundaries form a more effective barrier and no synthetic
444 faults cross-cut the central domain.

445 In comparison with the Series B and Series C models, the initial N20°W striking central domain boundaries
446 in the Series D models are the least favorably oriented for fault activation. In the weak-strong-weak Model
447 D1 (Fig. 8 e and f), the domain boundaries are not activated at all and the synthetic faults forming in the
448 outer domains propagate across the central domain. Apart from a slight re-orientation of the fault strike,
449 reflecting the difference in material strength between central and outer domains (difference in internal
450 friction angles), the fault pattern in Model D1 is very similar to the one in Model A1, which had no vertical
451 brittle strength contrasts. The strong-weak-strong Model D2 shows a different deformation behaviour.
452 Although the domain boundaries at the surface are not activated, the presence of a weak material surrounded
453 by strong material results in internal deformation within the central domain and dextral oblique-slip reverse
454 faults form striking parallel to the domain boundaries. These faults prevent synthetic faults from crossing
455 the central domain, and they halt against the oblique-slip reverse faults.

456 In all models with vertical domains of contrasting brittle strength, the orientation of the sinistral, synthetic
457 faults forming in the outer domains reflects the Mohr-Coulomb failure criterion, i.e. if the outer domains
458 consist of weak microbeads, with an internal friction angle of 22°, the strike of the synthetic faults is c.
459 N79°E and when the outer domains consist of strong quartz sand, with an internal friction angle of 36°, the
460 strike of the synthetic faults is c. N72°E (see also section 4.1). In those models, in which the synthetic faults
461 cross-cut the central domain, the strike of the faults changes slightly, due to the difference in internal friction
462 angles between the quartz sand and the microbeads (Du and Aydin, 1995; de Doney et al., 2011).

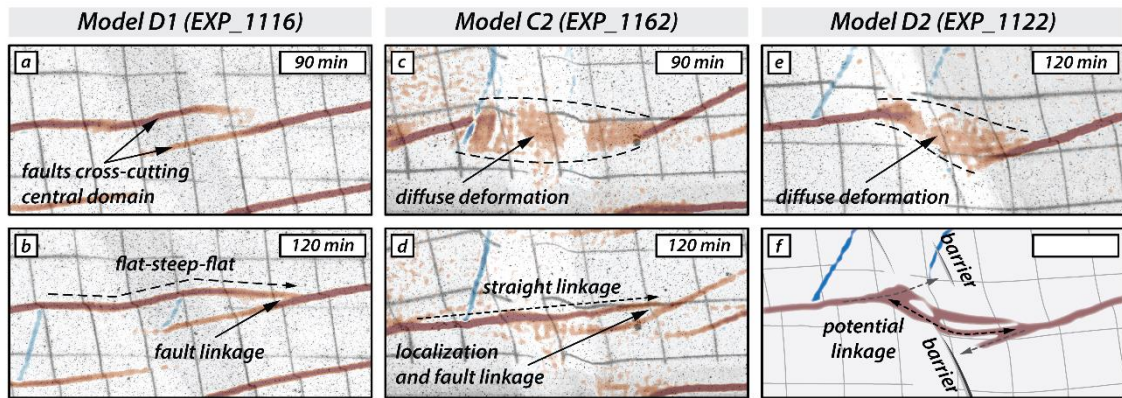
463 The antithetic faults that form in the outer domains of our models are of two types: (i) those that form
464 relatively early in as yet largely unfaulted domains and strike at large angles to the shear direction and (ii)
465 those confined between earlier formed and overlapping synthetic faults that strike at lower angles to the
466 shear direction. The early-formed dextral, antithetic faults reflect the orientation predicted by the Mohr-
467 Coulomb failure criterion, striking c. N18°E if the outer domains consist of quartz sand and c. N11°E if the
468 outer domains consist of microbeads. Due to lateral fault propagation and coeval rotation of the central fault
469 segments, these antithetic faults obtain a slightly S-shaped sigmoidal form in map view during progressive
470 simple shear (see also Schreurs, 1994, 2003; Dooley and Schreurs, 2012). The antithetic faults that are

471 confined in between closely spaced, earlier formed, synthetic faults have an initial different strike (c. N15°-
472 N20°E in microbeads domains, e.g. Model C1) and c. N25°-N30°E in quartz sand domains, (e.g. Model
473 C2), which is clearly different from those antithetic faults formed during early stages in largely unfaulted
474 domains. The antithetic faults confined between major synthetic faults result from local stress field
475 modifications governed by relative movement of material in between previously formed synthetic faults
476 with large overlap (Schreurs, 2003; Dooley and Schreurs, 2012; their R'_L faults). Both types of antithetic
477 faults rotate counterclockwise with progressive sinistral simple shear. Rotation of faults and blocks in
478 strike-slip fault systems is not only observed in analogue models (Schreurs, 1994, 2003; Dooley and
479 Schreurs, 2012), but has also been documented in nature (e.g., Ron et al., 1986; Nicholson et al., 1986). It
480 is thus important to keep in mind that antithetic faults (and blocks in between) can undergo considerable
481 rotation about a vertical axis during simple shear deformation, implying that present-day antithetic fault
482 orientations in strike-slip fault systems do not necessarily reflect the orientations in which they initially
483 formed.

484

485 **4.3. Fault linkage across central domain**

486 In models where synthetic faults from the eastern and western domain cross-cut the central domain, the
487 entire model behaves as one domain. As shown in the section above, this is the case for models C2, D1,
488 and D2 where the vertical boundaries of the central domain are not or only partially activated, depending
489 on the orientation of the central domain (section 4.2). However, all three models show distinct differences
490 in how laterally propagating synthetic strike-slip faults link across the central domain (Fig. 9). For model
491 D1 (Fig. 9a, b), faults cross-cut the stronger (i.e., quartz sand) central domain from the E and W domains
492 (Fig. 9a) and eventually link in the E domain (Fig. 9b). Across the central domain, the fault strike changes
493 according to the predicted Mohr-Coulomb failure criterion resulting in a step-like linkage pattern in surface
494 view (i.e., flat-steep-flat; Fig. 9a, b).



495

496 **Figure 9: Surface detailed photographs of the central domain of the models with the contrasting brittle**
 497 **mechanical strength, showing the fault linkage across the central domain at 90 minutes (60 mm displacement)**
 498 **and 120 minutes (80 mm displacement). a) and b) model D1 with the central domain striking N20°W and**
 499 **composed by the strong material (quartz). c) and d) model C2 with the central domain striking N-S and**
 500 **composed by the weak material (microbeads). e) model D2 with the central domain striking N20°W and**
 501 **composed by the weak material (microbeads). f) Schematic drawing for the fault linkage at the last stage.**

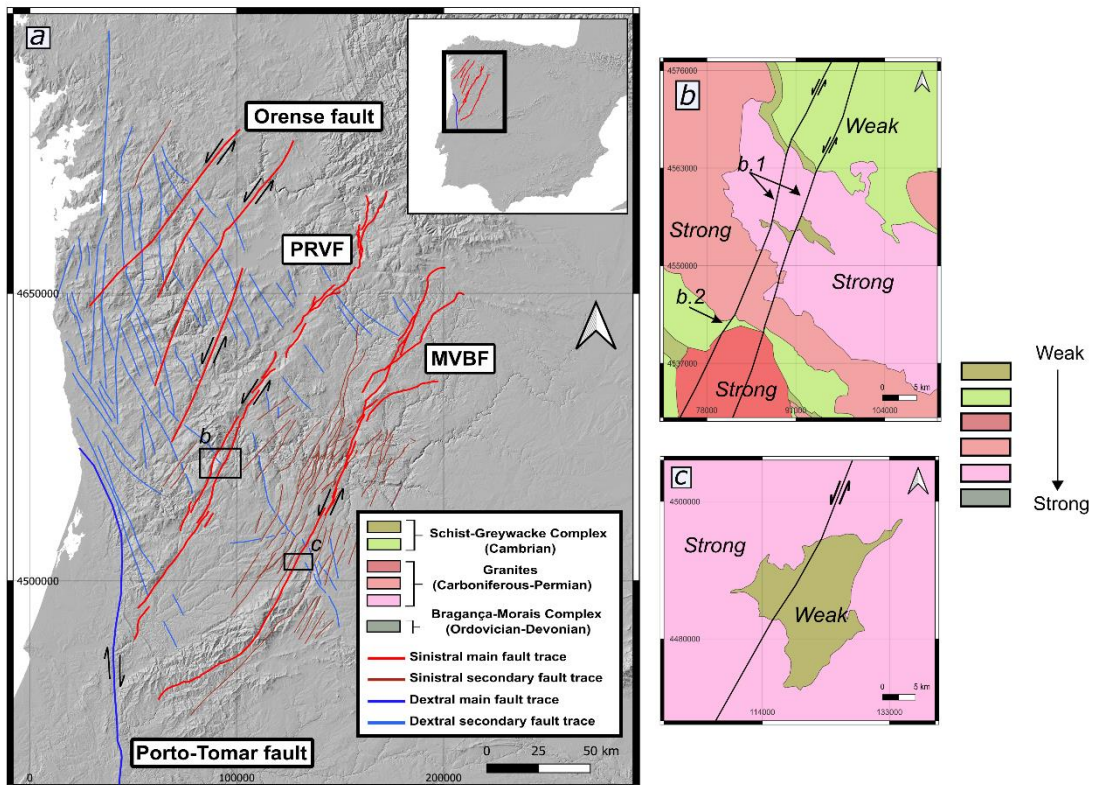
502

503 For models C2 and D2, however, the domain configuration strong-weak-strong has implications for fault
 504 linkage. As synthetic strike-slip faults propagate from the western and eastern domains towards the weaker
 505 central domain, early deformation patterns are characterized by a zone of diffuse deformation across the
 506 central domain (Fig. 9c, e). In model C2, the fault from the W domain cross-cuts the weak central domain
 507 and eventually links with the fault in the E domain in a straight fashion after 120 min (Fig. 9d), abandoning
 508 earlier active fault strands striking N18°E (i.e., the predicted orientation for Mohr-Coulomb failure
 509 criterion). Similar fault kinematics should be expected for model D2 (Fig. 9e, f). However, laterally
 510 propagating faults in the western and eastern domain do not link during the duration of the model run.
 511 Instead, the two fault segments halt at the domain boundary resulting in ongoing diffuse deformation
 512 without strain localization in the central domain. This behavior may be explained by the presence of the
 513 N20°W-striking reverse faults within the central model domain. Due to the misalignment between central
 514 domain boundaries and the expected orientation of antithetic faults, the domain boundaries do not activate
 515 and domain-internal deformation is taken up by oblique-slip dextral reverse faults. Such faults (i.e., nearly
 516 orthogonally striking with respect to synthetic faults) accommodate bulk shear deformation hindering the
 517 synthetic faults to propagate. In that sense, the oblique-slip reverse faults act as an impenetrable barrier
 518 inhibiting linkage of synthetic faults across the weak central domain (Fig. 9f). Oblique-slip reverse faults
 519 in the central domain, therefore, influence fault interaction across the central domain in a similar way as do
 520 the activated domain boundaries in models B1, B2, and C1 (Fig. 8).

521

522 **4.4. Comparison with strike-slip fault zones in Iberia**

523 The NW Iberian Peninsula contains major sinistral and dextral strike-slip intraplate fault systems (Fig. 10a).
524 These groups on intraplate fault systems are located in an old basement developed during Variscan Orogeny
525 (Devonian-Carboniferous, e.g., Matte, 1991; Martínez Catalán et al., 1997; Fernández et al., 2004), during
526 this stage a set of lithologic units with contrasting properties such as granites, quartzites, slates and high-
527 grade metamorphic rocks were emplaced and deformed. During the Alpine Compression (Late Cretaceous
528 to the present), the present fault pattern was obtained due to the collision between the Iberian microplate
529 and the northern edge of Africa in the middle Miocene (e. g., Alonso et al., 1996; Vegas et al., 2004; Martín-
530 González and Heredia, 2011, Martín-González et al., 2012). This collision caused the Iberian Peninsula to
531 undergo a counterclockwise twist, resulting in slight shearing (e.g. Martínez Catalán, 2011; Vergés et al.,
532 2019). In the study area, intraplate deformation led to a fault pattern primarily composed of sinistral faults,
533 such as the Penacova-Régua-Verin (PRVF), Manteigas-Vilaríça-Bragança (MVBF), and Orense faults (see
534 Fig. 10a). Additionally, antithetic dextral faults were also generated (see Fig. 10a).



535

536 **Figure 10: a) Digital elevation model of the northwest section of the Iberian Peninsula where the main faults**
537 **are drawn, with the location of Figures b and c. The faults are essentially sinistral and there is a dextral fault on**
538 **the southern edge that delimits the study area. In blue and light red, the secondary antithetic (dextral) and**
539 **synthetic (sinistral) faults have been marked respectively. b) Schematic representation of the southern section**
540 **of the Verin fault showing patterns of directional changes similar to models D1 and D2. c) Schematic**
541 **representation of the southern section of the Vilarica fault showing a similar deformation pattern to model C2.**

542

543 Among the traces of these faults, we can observe antithetic faults that do not connect with each other and,
544 in some cases, acquire an S shape as described in the C1 and C2 models (Fig. 8). These antithetical faults
545 are not in a conjugate position and are confined between the sinistral faults. At the end of the sinistral faults
546 is the Porto-Tomar fault, which delimits the study area. The Porto-Tomar fault shows dextral displacement
547 and tectonically delimits the area to the north and south of Portugal (Veludo et al., 2017). The main trace
548 of the sinistral faults is not completely straight and undergoes small changes that are observable at a larger
549 scale (Fig. 10b and c). Along the same trace of the PRV fault, it is observed that the faults undergo a
550 counterclockwise refraction, similar to the D1 model with quartz in the central domain (Fig. 10b). On the
551 other hand, in section b.2, the fault undergoes a clockwise refraction as it crosses shale-type materials
552 (which is represented by the microbeads grains in our models; Panien et al., 2006), similar to the D2
553 experiment. This phenomenon is also observed in the Vilarica fault when the fault intersects granites and
554 slates units (Fig. 10c).

555

556 **5. Conclusions**

557 We performed a series of analogue models to investigate faulting in the upper, brittle crust as a result of
558 sinistral simple shear. The initial model had a rectangular shape with the long axis parallel to the shear
559 direction. In two reference models, the brittle crust consisted of either a weak granular material
560 (microbeads) or a strong granular material (quartz sand). In a further six models, we introduced mechanical
561 strength contrasts in the upper crust, by introducing a vertical central domain consisting of quartz sand
562 surrounded by microbeads (i.e. a weak-strong-weak configuration) or the other way around (i.e. a strong-
563 weak-strong configuration). These models allowed us to test the influence of vertical domains of contrasting
564 brittle strength on the fault pattern, and the influence of the weak-strong-weak and strong-weak-strong
565 configuration.

- 566 - The fault pattern of models with a single granular material simulating the upper crust (i.e. no vertical
567 domains of contrasting brittle mechanical strength) is dominated by sinistral (synthetic) strike-slip
568 faulting, whose orientations are readily explained by the Mohr-Coulomb failure criterion, with fault
569 strikes being a function of the internal friction angles, which differ between microbeads ($\phi=22^\circ$) and
570 quartz sand ($\phi=36^\circ$)
- 571 - In models with vertical domains of contrasting brittle strength, initial fault development occurs in the
572 outer domains with syn- and antithetic faults forming in the expected orientations according to the
573 Mohr-Coulomb failure criterion.
- 574 - In models with domains of contrasting brittle strength, the central domain boundaries are almost
575 completely or fully activated if their strike orientation is subparallel to the predicted antithetic fault
576 orientation. As a consequence, faulting occurs in three distinct structural domains.
- 577 - If the orientation of the domain boundaries is less favorably oriented, they are only partially activated
578 or not at all, allowing synthetic faults that form in the outer domains to cut across the central domain.
579 Hence, there are no distinct structural domains.
- 580 - If the central domain boundaries are fully activated and three structurally distinct domains form, the
581 strength contrast between the domains (i.e. weak-strong-weak or strong-weak-strong) does not
582 influence the overall fault pattern. However, if the domain boundaries remain inactive then the strength
583 contrast between the domains has an influence on the fault development and evolution. In the case of
584 weak-strong-weak, the synthetic faults from the outer domains cross-cut the central domain with a
585 slight change in strike orientation, whereas in the case of strong-weak-strong, the weak central domain
586 show internal oblique-slip reverse faulting, which inhibits faults from the outer domain to fully cross
587 the central domain.
- 588 - Although we only tested sinistral simple shear, our results can also be applied to dextral simple shear
589 by mirroring the fault patterns around a N-S axis.
- 590 - Our results are comparable with the fault systems observed in the NW of the Iberian Peninsula. The
591 area shows synthetic and antithetic faults whose distribution is similar to the models made. In addition,
592 refraction patterns of the main trace of the faults associated with lithological contrasts can be observed.
- 593
- 594

595 **6. Competing interests**

596 The contact author has declared that none of the authors has any competing interests.

597 **7. Acknowledgments**

598 The following work has been partially funded by a predoctoral contract (PREDOC20-073), by the
599 Universidad Rey Juan Carlos and project PID2022-139527OB-I00 funded by
600 MCIN/AEI/10.13039/501100011033/ and FEDER.

601

602 **8. References**

- 603 Alonso, J. L., Pulgar, J. A., García-Ramos, J. C., & Barba, P.: Tertiary basins and Alpine tectonics in the
604 Cantabrian Mountains (NW Spain). in *Tertiary Basins of Spain* (pp. 214–227). Cambridge
605 University Press. 1996
- 606 Aki, K.: Geometric features of a fault zone related to the nucleation and termination of an earthquake
607 rupture, in: *Proceedings of Conference XLV Fault Segmentation and Controls of Rupture Initiation*
608 and Termination. US Geological Survey Open File Report 89-315, pp. 1–9, 1989
- 609 Arthaud, F., Matte, Ph.: Les décrochements tardi-hercyniens du sud-ouest de l'europe. *Geometrie et essai*
610 *de reconstitution des conditions de la deformation. Tectonophysics* 25, 139–171.
611 [https://doi.org/10.1016/0040-1951\(75\)90014-1](https://doi.org/10.1016/0040-1951(75)90014-1), 1975.
- 612 Anderson, E. M: *The Dynamics of faulting and Dyke Formation with Applications to Britain* (2nd edition),
613 Oliver and Boyd, Edinburgh, Scotland, 1951.
- 614 Antonellini, M.A., Aydin, A., Pollard, D.D.: Microstructure of deformation bands in porous sandstones at
615 Arches National Park, Utah. *Journal of Structural Geology* 16, 941e959, 1994.
- 616 Aydin, A., Nur, A.: Evolution of pull-apart basins and their scale independence. *Tectonics* 1, 91–105, 1982.
- 617 Aydin, A.: Fractures, faults, and hydrocarbon entrapment, migration and flow. *Marine and Petroleum*
618 *Geology* 17, 797–814, 2000.
- 619 Aydin, A., & Berryman, J. G: Analysis of the growth of strike-slip faults using effective medium
620 theory. *Journal of Structural Geology*, 32(11), 1629–1642.
621 <https://doi.org/10.1016/j.jsg.2009.11.007>, 2010.
- 622 Barka, A., Kadinsky-Cade, K.: Strike-slip fault geometry in Turkey and its influence on earthquake activity.
623 *Tectonics* 7, 663–684, 1988.
- 624 [Boutelier, D., Schrank, C., Regenauer-Lieb, K.: 2-D finite displacements and strain from particle imaging](#)
625 [velocimetry \(PIV\) analysis of tectonic analogue models with TecPIV. *Solid Earth* 10, 1123-1139,](#)
626 [2019.](#)
- 627 Burgmann, R., Pollard, D.D.: Strain accommodation about strike-slip fault discontinuities in granitic rock
628 under brittle-to-ductile conditions. *Journal of Structural Geology* 16, 1655–1674, 1994.
- 629 Cazarin, C.L., van der Velde, R., Santos, R.V., Reijmer, J.J.G., Bezerra, F.H.R., Bertotti, G., La Bruna, V.,
630 Silva, D.C.C., de Castro, D.L., Srivastava, N.K., Barbosa, P. F.: Hydrothermal activity along a
631 strike-slip fault zone and host units in the São Francisco Craton, Brazil – implications for fluid
632 flow in sedimentary basins. *Precambrian Res.* 365
633 <https://doi.org/10.1016/j.precamres.2021.106365>, 2021.
- 634 Cheng, X., Ding, W., Pan, L., Zou, Y., Li, Y., Yin, Y., & Ding, S.: Geometry and kinematics characteristics
635 of strike-slip fault zone in complex structure area: A case study from the south no. 15 strike-slip
636 fault zone in the Eastern Sichuan Basin, China. *Frontiers in earth science*, 10.
637 <https://doi.org/10.3389/feart.2022.922664>, 2022.

- 638 [Cooke, M. L., Toeneboehn, K., and Hatch, J. L.: Onset of slip partitioning under oblique convergence](#)
639 [within scaled physical experiments, *Geosphere*, 16, 875-889. <https://doi.org/10.1130/GES02179.1>,](#)
640 [2020.](#)
- 641 [de Jossineau, G., & Aydin, A.: Segmentation along strike-slip faults revisited. *Pure and Applied*](#)
642 [Geophysics, 166\(10–11\), 1575–1594. <https://doi.org/10.1007/s00024-009-0511-4>, 2009.](#)
- 643 Deng, Q., Wu, D., Zhang, P., & Chen, S.: Structure and deformational character of strike-slip fault zones.
644 *Pure and Applied Geophysics*, 124(1–2), 203–223. <https://doi.org/10.1007/bf00875726>, 1986.
- 645 Díez Fernández, R., Pereira, M.F.: Extensional orogenic collapse captured by strike-slip tectonics:
646 Constraints from structural geology and UPb geochronology of the Pinhel shear zone (Variscan
647 orogen, Iberian Massif). *Tectonophysics* 691, 290–310.
648 <https://doi.org/10.1016/j.tecto.2016.10.023>, 2016.
- 649
- 650 [Dooley, T. P., & Schreurs, G. : Analogue modelling of intraplate strike-slip tectonics: A review and new](#)
651 [experimental results. *Tectonophysics*, 574–575, 1–71. <https://doi.org/10.1016/j.tecto.2012.05.030>,](#)
652 [2012](#)
- 653 Du, Y., & Aydin, A.: Shear fracture patterns and connectivity at geometric complexities along strike-slip
654 faults. *Journal of Geophysical Research*, 100(B9), 18093–18102.
655 <https://doi.org/10.1029/95jb01574>, 1995.
- 656 Fernández, M., Marzán, I., & Torne, M.: Lithospheric transition from the Variscan Iberian Massif to the
657 Jurassic oceanic crust of the Central Atlantic. *Tectonophysics*, 386(1–2), 97–115.
658 <https://doi.org/10.1016/j.tecto.2004.05.005>, 2004
- 659 Gabrielsen, R. H., Giannenas, P. A., Sokoutis, D., Willingshofer, E., Hassaan, M., & Faleide, J. I.:
660 Analogue experiments on releasing and restraining bends and their application to the study of the
661 Barents Shear Margin. *Solid Earth*, 14(9), 961–983. <https://doi.org/10.5194/se-14-961-2023>, 2023
- 662 Gamond, J.F.: Displacement features associated with fault zones: a comparison between observed examples
663 and experimental models. *Journal of Structural Geology* 5, 33–45, 1983.
- 664 Garfunkel, Z., & Ron, H.: Block rotation and deformation by strike-slip faults: 2. The properties of a type
665 of macroscopic discontinuous deformation. *Journal of Geophysical Research*, 90(B10), 8589–8602.
666 <https://doi.org/10.1029/jb090i10p08589>, 1985.
- 667 Gomes, A. S., Rosas, F. M., Duarte, J. C., Schellart, W. P., Almeida, J., Tomás, R., & Strak, V.: Analogue
668 modelling of brittle shear zone propagation across upper crustal morpho-rheological
669 heterogeneities. *Journal of Structural Geology*, 126, 175–197.
670 <https://doi.org/10.1016/j.jsg.2019.06.004>, 2019.
- 671 Gutiérrez-Alonso, G., Collins, A. S., Fernández-Suárez, J., Pastor-Galán, D., González-Clavijo, E.,
672 Jourdan, F., Weil, A. B., & Johnston, S. T.: Dating of lithospheric buckling: 40Ar/39Ar ages of
673 syn-orocline strike-slip shear zones in northwestern Iberia. *Tectonophysics*, 643, 44–54.
674 <https://doi.org/10.1016/j.tecto.2014.12.009>, 2015.
- 675 Harris, R.A., Day, S.M.: Dynamic 3D simulation of earthquakes on en echelon faults. *Geophysical*
676 *Research Letters* 26, 2089–2092, 1999.
- 677 Hubbert, M. K.: Theory of scale models as applied to the study of geologic structures. *The Geological*
678 *Society of America Bulletin*, 48(10), 1459–1520. <https://doi.org/10.1130/GSAB-48-1459>, 1937.
- 679 Kavyani-Sadr, K., Rahimi, B., Khatib, M.M., Kim, Y.-S.: Assessment of open spaces related to Riedel-
680 shears dip effect in brittle shear zones. *J. Struct. Geol.* 154, 104486
681 <https://doi.org/10.1016/j.jsg.2021.104486>, 2022.
- 682 Kim, Y., Peacock, D.C.P., Sanderson, D.J.: Fault damage zones. *Journal of Structural Geology* 26, 503–
683 517, 2004.
- 684 Kirkland, C. L., Alsop, G. I., & Prave, A. R.: The brittle evolution of a major strike-slip fault associated
685 with granite emplacement: a case study of the Leannan Fault, NW Ireland. *Journal of the Geological*
686 *Society*, 165(1), 341–352. <https://doi.org/10.1144/0016-76492007-064>, 2008.
- 687 [Lefevre, M., Souloumiac, P., Cubas, N., & Klinger, Y. : Experimental evidence for crustal control over](#)
688 [seismic fault segmentation. *Geology*, 48\(8\), 844–848. <https://doi.org/10.1130/g47115.1>, 2020.](#)
- 689 Livio, F. A., Ferrario, M. F., Frigerio, C., Zerboni, A., & Michetti, A. M.: Variable fault tip propagation
690 rates affected by near-surface lithology and implications for fault displacement hazard assessment.
691 *Journal of Structural Geology*, 130(103914), 103914. <https://doi.org/10.1016/j.jsg.2019.103914>,
692 2020.

- 693 Mair, K., Frye, K.M., Marone, C.: Influence of grain characteristics on the friction of granular shear zones.
694 *Journal of Geophysical Research* 107 (B10), 4/1-4/9, 2002.
- 695 Matte, P.: Accretionary history and crustal evolution of the Variscan belt in Western
696 Europe. *Tectonophysics*, 196(3–4), 309–337. [https://doi.org/10.1016/0040-1951\(91\)90328-p](https://doi.org/10.1016/0040-1951(91)90328-p). 1991.
- 697 Martel, S.J., Peterson Jr., J.E.: Interdisciplinary characterization of fracture systems at the US/BK site,
698 Grimsel Laboratory, Switzerland. *International Journal of Rock Mechanics and Mining Science and*
699 *Geomechanical Abstracts* 28, 259–323, 1991.
- 700 Martínez Catalán, J. R., Arenas, R., Díaz García, F., & Abati, J.: Variscan accretionary complex of
701 northwest Iberia: Terrane correlation and succession of tectonothermal events. *Geology*, 25(12),
702 1103. [https://doi.org/10.1130/0091-7613\(1997\)025<1103:vaconi>2.3.co;2](https://doi.org/10.1130/0091-7613(1997)025<1103:vaconi>2.3.co;2). 1997
703
- 704 Martínez Catalán, J.R. : The Central Iberian arc, an orocline centered in the Iberian Massif and some
705 implications for the Variscan belt. *Int. J. Earth Sci.* 101, 1299–1314.
706 <https://doi.org/10.1007/s00531-011-0715-6>, 2012.
- 707 Martín-González, F., Heredia, N.: Geometry, structures and evolution of the western termination of the
708 Alpine-Pyrenean Orogen reliefs (NW Iberian Peninsula). *J. Iber. Geol.* 37, 103–120.
709 https://doi.org/10.5209/rev_JIGE.2011.v37.n2.1, 2011.
- 710 Martín-González, F., Barbero, L., Capote, R., Heredia, N., & Gallastegui, G.: Interaction of two successive
711 Alpine deformation fronts: constraints from low-temperature thermochronology and structural
712 mapping (NW Iberian Peninsula). *International Journal of Earth Sciences*, 101(5), 1331–1342.
713 <https://doi.org/10.1007/s00531-011-0712-9>. 2012.
714
- 715 Moore, J. D. P., & Parsons, B.: Scaling of viscous shear zones with depth-dependent viscosity and power-
716 law stress–strain-rate dependence. *Geophysical Journal International*, 202(1), 242–260.
717 <https://doi.org/10.1093/gji/ggv143>, 2015.
- 718 Myers, R., Aydin, A.: The evolution of faults formed by shearing across joint zones in sandstone. *Journal*
719 *of Structural Geology* 26, 947–966, 2004.
- 720 Nicholson, C., Seeber, L., Williams, P. and Sykes, L.R.: Seismic evidence for conjugate slip and block
721 rotation within the San Andreas fault system, Southern California. *Tectonics*, 5: 629-648, 1986
- 722 Odling, N.E., Harris, S.D., Knipe, R.J.: Permeability scaling properties of fault damage zones in siliclastic
723 rocks. *Journal of Structural Geology* 26, 1727–1747, 2004.
- 724 Panien, M., Schreurs, G., & Pfiffner, A.: Mechanical behaviour of granular materials used in analogue
725 modelling: insights from grain characterisation, ring-shear tests and analogue experiments. *Journal*
726 *of Structural Geology*, 28(9), 1710–1724. <https://doi.org/10.1016/j.jsg.2006.05.004>, 2006.
- 727 Peacock, D.C.P., Sanderson, D.J.: Displacement, segment linkage and relay ramps in normal fault zones.
728 *Journal of Structural Geology* 13, 721–733, 1991.
729
- 730 Peacock, D. C. P., & Sanderson, D. J.: Effects of layering and anisotropy on fault geometry. *Journal of the*
731 *Geological Society*, 149(5), 793–802. <https://doi.org/10.1144/gsjgs.149.5.0793>, 1992.
- 732 Petersen, M. D., Dawson, T. E., Chen, R., Cao, T., Wills, C. J., Schwartz, D. P., & Frankel, A. D.: Fault
733 displacement hazard for strike-slip faults. *Bulletin of the Seismological Society of America*, 101(2),
734 805–825. <https://doi.org/10.1785/0120100035>, 2011.
- 735 Preuss, S., Herrendörfer, R., Gerya, T., Ampuero, J.-P., & Dinther, Y.: Seismic and aseismic fault growth
736 lead to different fault orientations. *Journal of Geophysical Research. Solid Earth*, 124(8), 8867–
737 8889. <https://doi.org/10.1029/2019jb017324>, 2019.
- 738 Ramberg, H.: Gravity, deformation and the Earth's crust: In theory, experiments and geological application
739 (p. 452). Academic Press, 1981.
- 740 Richard, P.: Experiments on faulting in a two-layered cover sequence overlying a reactivated basement
741 fault with oblique-slip. *J. Struct. Geol.* 13, 459–469, 1991.
- 742 Richard, P., Naylor, M.A., Koopman, A.: Experimental models of strike-slip tectonics. *Petroleum*
743 *Geoscience* 1, 71–80, 1995.
- 744 Rispoli, R.: Stress fields about strike-slip faults inferred from stylolites and tension gashes. *Tectonophysics*
745 75, 729–736, 1981.
- 746 Ron, H., Freund, R., Garfunkel, Z. and Nur, A.: Block rotation by strike slip faulting: structural and
747 paleomagnetic evidence. *J. Geophys. Res.*, 89: 6256-6270, 1984.

- 748 [Schellart, W.P., Strak, V.: A review of analogue modelling of geodynamic processes: Approaches, scaling,](#)
749 [materials and quantification, with an application to subduction experiments. *J. Geodyn.* 100, 7–32.](#)
750 <https://doi.org/10.1016/j.jog.2016.03.009>, 2016.
- 751 [Schmid, T., Schreurs, G., Warsitzka, M., & Rosenau, M.: Effect of sieving height on density and friction of](#)
752 [brittle analogue material: Ring-shear test data of quartz sand used for analogue experiments in the](#)
753 [Tectonic Modelling Lab of the University of Bern. *GFZ Data Services.*](#)
754 <https://doi.org/10.5880/fidgeo.2020.006>, 2020.
- 755 [Schmid, T. C., Schreurs, G., & Adam, J.: Rotational extension promotes coeval upper crustal brittle faulting](#)
756 [and deep-seated rift-axis parallel flow: Dynamic coupling processes inferred from analog model](#)
757 [experiments. *Journal of Geophysical Research. Solid Earth*, 127\(8\).](#)
758 <https://doi.org/10.1029/2022jb024434>, 2022.
- 759 [Schmid, T. C., Brune, S., Glerum, A., & Schreurs, G.: Tectonic interactions during rift linkage: Insights](#)
760 [from analog and numerical experiments. <https://doi.org/10.5194/egusphere-2022-1203>, 2023](#)
- 761 Scholz, C. H.: *The Mechanics of Earthquakes and Faulting*. Cambridge University Press, 2002.
- 762 Segall, P., & Pollard, D. D.: Nucleation and growth of strike slip faults in granite. *Journal of Geophysical*
763 *Research*, 88(B1), 555. <https://doi.org/10.1029/jb088ib01p00555>, 1983.
- 764 Shaw, B.E., Dieterich, J.H.: Probabilities for jumping fault segment stepovers. *Geophysical Research*
765 *Letters* 34, L01307. doi:10.1029/2006GL027980, 2007.
- 766 Sibson, R.H.: Stopping of earthquake ruptures at dilational fault jogs. *Nature* 316, 248–251, 1985.
- 767 Stirling, M.W., Wesnousky, S.G., Shimazaki, K.: Fault trace complexity, cumulative slip, and the shape of
768 the magnitude-frequency distribution for strike-slip faults: a global survey. *Geophysical Journal*
769 *International* 124, 833–868, 1996.
- 770 Sylvester, A.G.: Strike-slip faults. *Geol. Soc. Am. Bull.* 100, 1666–1703. [https://doi.org/10.1130/0016-](https://doi.org/10.1130/0016-7606(1988)1002.3.CO;2)
771 [7606\(1988\)1002.3.CO;2](https://doi.org/10.1130/0016-7606(1988)1002.3.CO;2), 1988.
- 772 Vegas, R., Vicente Muñoz, G., Muñoz Martín, A., & Palomino, R.: *Los corredores de fallas de Réguar-*
773 *Verin y Vilariça: Zonas de transferencia de la deformación intraplaca en la Península Ibérica*. 2004
- 774 Veludo, I., Dias, N. A., Fonseca, P. E., Matias, L., Carrilho, F., Haberland, C., & Villaseñor, A.: Crustal
775 seismic structure beneath Portugal and southern Galicia (Western Iberia) and the role of Variscan
776 inheritance. *Tectonophysics*, 717, 645–664. <https://doi.org/10.1016/j.tecto.2017.08.018>. 2017
- 777 Venâncio, M. B., & da Silva, F. C. A.: Structures evolution along strike-slip fault zones: The role of
778 rheology revealed by PIV analysis of analog modeling. *Tectonophysics*, 229764, 229764.
779 <https://doi.org/10.1016/j.tecto.2023.229764>, 2023.
- 780 Vergés, J., Kullberg, J. C., Casas-Sainz, A., de Vicente, G., Duarte, L. V., Fernández, M., Gómez, J. J.,
781 Gómez-Pugnaire, M. T., Jabaloy Sánchez, A., López-Gómez, J., Macchiavelli, C., Martín-Algarra,
782 A., Martín-Chivelet, J., Muñoz, J. A., Quesada, C., Terrinha, P., Torné, M., & Vegas, R.: An
783 introduction to the alpine cycle in Iberia. En *The Geology of Iberia: A Geodynamic Approach* (pp.
784 1–14). Springer International Publishing. 2019
- 785 Viola, G., Odonne, F., Mancktelow, N.S.: Analogue modelling of reverse fault reactivation in strike-slip
786 and transpressive regimes: application to the Giudicarie fault system, Italian Eastern Alps. *J. Struct.*
787 *Geol.* 36, 401–418. <https://doi.org/10.1016/j.jsg.2003.08.014>, 2004.
- 788 Wesnousky, S.G.: Seismological and structural evolution of strike-slip faults. *Nature* 335, 340–342, 1988.
- 789 Wesnousky, S.G.: Predicting the endpoints of earthquake ruptures. *Nature* 444, 358–360, 2006.
- 790 [Westerweel, J., Scarano, F.: Universal outlier detection for PIV data. *Experiments in fluids* 39, 1096-1100,](#)
791 [2005.](#)
- 792 Zwaan, F., Schreurs, G., Ritter, M., Santimano, T., & Rosenau, M.: Rheology of PDMS-corundum sand
793 mixtures from the Tectonic Modelling Lab of the University of Bern (CH). V. 1. *GFZ data Services.*
794 <https://doi.org/10.5880/fidgeo.2018.023>, 2018.
- 795 Zwaan, F., Schreurs, G., Gentzmann, R., Warsitzka, M. & Rosenau, M. Ring-shear test data of quartz sand
796 from the Tectonic Modelling Lab of the University of Bern (CH). *GFZ Data Services,*
797 <http://doi.org/10.5880/fidgeo.2018.028>

798 Zwaan, F., Schreurs, G., Madritsch, H., & Herwegh, M.: Influence of rheologically weak layers on fault
799 architecture: insights from analogue models in the context of the Northern Alpine Foreland Basin.
800 Swiss Journal of Geosciences, 115(1). <https://doi.org/10.1186/s00015-022-00427-8>, 2022.